Research Article | Vol. 12, No. 1 / 1 January 2021 / Biomedical Optics Express 110
Biomedical Optics EXPRESS

Intrinsic spectrally-dependent background in spectroscopic visible-light optical coherence tomography

IAN RUBINOFF,[1] ROMAN V. KURANOV,[1,2] AND HAO F. ZHANG[1,*]

[1]Department of Biomedical Engineering, Northwestern University, Evanston, IL 60208, USA
[2]Opticent Health, Evanston, IL 60201, USA
[*]hfzhang@northwestern.edu

Abstract: Visible-light optical coherence tomography (vis-OCT) has enabled new spectroscopic applications, such as retinal oximetry, as a result of increased optical absorption and scattering contacts in biological tissue and improved axial resolution. Besides extracting tissue properties from back-scattered light, spectroscopic analyses must consider spectral alterations induced by image reconstruction itself. We investigated an intrinsic spectral bias in the background noise floor, which is hereby referred to as the spectrally-dependent background (SDBG). We developed an analytical model to predict the SDBG-induced bias and validated this model using numerically simulated and experimentally acquired data. We found that SDBG systemically altered the measured spectra of blood in human retinal vessels in vis-OCT, as compared to literature data. We provided solutions to quantify and compensate for SDBG in retinal oximetry. This work is particularly significant for clinical applications of vis-OCT.

1. Introduction

Optical coherence tomography (OCT) [1] detects back-scattered light to image biological tissue at microscopic resolutions noninvasively. In spectral-domain OCT (SD-OCT) [2], three-dimensional (3D) images are reconstructed using the Discrete Fourier transform (DFT) of a sampled interference spectrum. Visible-light OCT (vis-OCT) [3] is a rapidly evolving SD-OCT technology that operates within the visible-light wavelength range to increase axial resolution and spectroscopic tissue contrast, as compared with near-infrared OCT (NIR-OCT). These benefits enabled new spectroscopic vis-OCT applications, including oximetry [4,5], detection of tissue ultrastructure [6], and investigating various neuropathologies [7,8]. Spectroscopic vis-OCT computes a series of short-time Fourier Transforms (STFT) using moving spectral windows with reduced bandwidth across the entire spectral interference fringes. Performing STFT enables the reconstruction of a series of sub-band spectral images with a reduced axial resolution.

To accurately extract tissue spectral information, it is essential to eliminate influence from the OCT image reconstruction itself. In most SD-OCTs, a grating-based spectrometer samples the interference fringe according to the grating equation and spectrometer optics [9]. It is typical for such spectrometers to sample almost linearly in the wavelength (λ) space, which is inversely proportional to the wavenumber (k) space. Since axial depth (z) is the Fourier conjugate of k, non-uniformly sampled frequencies in the k domain will result in a broadened point-spread-function in the z domain. Thus, the optimal axial resolution requires the interference fringe to be interpolated linearly in k space [2,10]. We found that linear-in-k interpolation generates spectrally-dependent background (SDBG), an intrinsic bias of the vis-OCT background noise floor that can alter spectroscopic measurements.

The prevalence of linear-in-k interpolation in SD-OCT makes the systemic nature of the SDBG highly significant towards the spectroscopic OCT research community. Various background biases have been previously reported [11–15]. For example, in polarization-sensitive OCT

#410011 https://doi.org/10.1364/BOE.410011
Journal © 2021 Received 11 Sep 2020; revised 15 Nov 2020; accepted 16 Nov 2020; published 8 Dec 2020

Biomedical Optics EXPRESS

(PS-OCT) the noise floor may vary in different polarization channels and, therefore, comparing the polarization channels may require noise floor correction to achieve more accurate PS-OCT data [12]. Although researchers previously recognized the existence of SDBG and applied empirical corrections [1315], a thorough investigation of SDBG's origin, influence on spectroscopic vis-OCT, and correction techniques have yet to be conducted.

In this work, we first theoretically derive the systemic bias of SDBG caused by linear-in-k interpolation of the interference fringe. We simulate SDBG in our vis-OCT system and compare it with experimentally acquired SDBG. Then, we establish a minimum fringe upsampling rate in spectroscopic vis-OCT that removes many depth-dependences of the SDBG, increasing simplicity of SDBG correction. Finally, we investigate the influence of SDBG on vis-OCT retinal oximetry and apply an SDBG correction strategy. This work establishes important principles and consequences of widely-used data processing in spectroscopic vis-OCT and all other SD-OCTs, informing a broad range of biophotonic applications.

2. Origin and derivation of SDBG

2.1. Wavenumber dispersion in spectrometer detection

In SD-OCT, the noise-free interference fringe (neglecting the DC component) can be written as

$$S(k)_{int} = \int_0^{z_{max}} 2\sqrt{S_{samp}(k,z)S_{ref}(k)}\cos(2kz)dz, \tag{1}$$

where z is the depth of the collected back-scattered photons from the zero-delay; z_{max} is the maximum imaging depth [16]; $S_{samp}(k,z)$ is the power spectrum of the back-scattered light from the depth z; and $S_{ref}(k)$ is the power spectrum of the reference arm. $S(k)_{int}$ is spatially dispersed onto a one-dimensional (1D) pixel array in the spectrometer as a function of $k(x)$ across the range from k_{start} to k_{end}, which is determined by the grating equation and spectrometer optics [9]. Here, x is the spatial coordinate along the 1D array ranging from 0 to $N\Delta x$, where N is the the total number of pixels and Δx is the width of each pixel.

The spatial dispersion of the spectrometer is represented by $\delta k = \left|\frac{dk(x)}{dx}\right|$, which we refer to as the k spacing. It is also important to consider a hypothetical uniform dispersion across the same spectral range, $\delta k_{lin} = \frac{|k_{end}-k_{start}|}{N\Delta x}$, which is constant. The dimensionless ratio, $\delta k_{rel} = \frac{\delta k}{\delta k_{lin}}$, referred to as relative k spacing, describes how the spectrometer deviates from ideal uniform k dispersion across each pixel. Indeed, a larger δk_{rel} indicates more k-space bandwidth per unit pixel Δx, while a smaller δk_{rel} indicates less k-space bandwidth per unit pixel. The interference fringe in the Eq. (1) sampled by the 1D pixel array (without considering spectrometer roll-off [17]) can be written as

$$S[j]_{int} = \sum_{j=1}^{N} S\left(x\frac{1}{\delta k_{rel}}\right)_{int}\theta(x-j\Delta x), \tag{2}$$

where $j = 1,\ 2,\ \ldots N$ is the array pixel index, and $\theta(x-j\Delta x)$ is the Dirac comb function with a period Δx. The spectrometer pixel array samples with a uniform period in x, but the fringe is a function of $\frac{1}{\delta k_{rel}}$. Such a non-uniform sampling of the k space results in a phase nonlinearity in $S[j]_{int}$ [18], which distorts $S[j]_{int}$ and reduces image axial resolution. For optimal image reconstruction, the phase of $S[j]_{int}$ must be made linear-in-k, which we will discuss in Section 2.2.

Quantifying $\frac{1}{\delta k_{rel}}$ for a spectrometer is valuable for understanding the distortion of $S[j]_{int}$. In this work, we measured $\frac{1}{\delta k_{rel}}$ digitally sampled by the spectrometer: $\frac{1}{\Delta k_{rel}}$. From here on, δk_{rel}. refers to the k spacing in the continuous domain, while Δk_{rel} refers to the k spacing in the discrete domain. Briefly, we found the k distribution on the pixel array $k[j]_{map}$ using spectral calibration lamps [17,18]. Next, we obtained the sampled δk, defined as Δk, by calculating the absolute

Biomedical Optics EXPRESS

change in $k[j]_{map}$ with j. Hence, the sampled δk_{lin} is

$$\Delta k_{lin} = \left| \frac{k[N]_{map} - k[1]_{map}}{N} \right|. \tag{3}$$

From this information, we obtained the sampled δk_{rel}, defined as $\Delta k_{rel} = \frac{\Delta k}{\Delta k_{lin}}$.

In Fig. 1(a), we plot measured $\frac{1}{\Delta k_{rel}}$ and $\frac{1}{\Delta k_{lin}}$ as a function of pixel j for a commercial vis-OCT spectrometer (Blizzard SR, Opticent Health, Evanston, IL.) Briefly, the spectrometer collimates light from a single-mode fiber output. The collimated light is diffracted by a transmission grating. The diffracted light is focused on a 2048-pixel camera (OctoPlus, Teledyne E2V, UK) placed at the focal plane of the diffracted light. The spectral detection range is from 506 nm to 613 nm. We measured the full spectrum roll-off as -4.8 dB/mm and confirmed that aberrations at the focal plane were minimized by measuring the spectrally-dependent roll-off (SDR) [17].

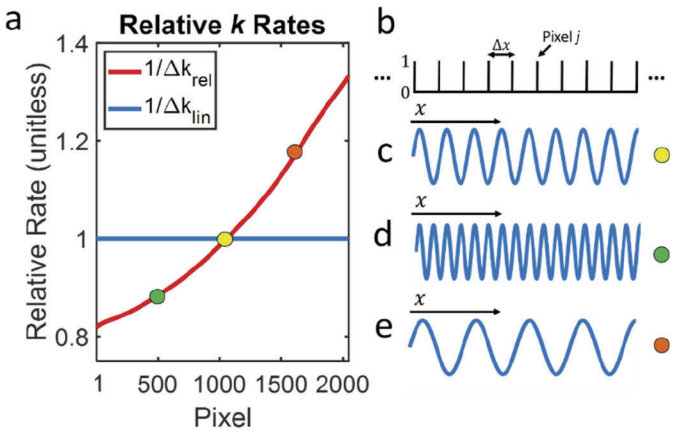

Fig. 1. Influence of grating dispersion on interference fringe (a) Digitized relative k rates of a spectrometer. Colored dots represent locations of pixel segments in (c-e); (b) illustration of Dirac comb sampling by pixel array with period Δx; (c) Interference fringe plotted at the location of the yellow dot in panel a; (d) Interference fringe plotted at the location of the green dot in panel a; (e) Interference fringe plotted at the location of the orange dot in panel a.

From Fig. 1(a), is evident that $\frac{1}{\Delta k_{rel}}$ is smaller for shorter wavelengths and larger for longer wavelengths. Physically, this can be considered as a compression of the k-space for shorter wavelengths and an expansion of the k-space for longer wavelengths, as shown in Figs. 1(b)–1(e). Figure 1(b) shows a segment of the Dirac Comb from Eq. (2), representing sampling by 10 pixels with a period of Δx. Figure 1(c) shows a single sine wave, representing a segment of $S\left(x\frac{1}{\delta k_{rel}}\right)_{int}$, where $\frac{1}{\delta k_{rel}} = \frac{1}{\delta k_{lin}}$ (highlighted by the yellow dot in Fig. 1(a)). All sine waves are plotted along the same x-axis from Fig. 1(b). Figure 1(d) shows the same $S\left(x\frac{1}{\delta k_{rel}}\right)_{int}$ as in Fig. 1(c), but for a segment where $\frac{1}{\delta k_{rel}} < \frac{1}{\delta k_{lin}}$ (highlighted by the green dot in Fig. 1(a)). This condition causes a compression of the k-space. Therefore, more cycles of $S\left(x\frac{1}{\delta k_{rel}}\right)_{int}$ are observed comparing with Fig. 1(c). Since the pixel array samples with uniform period Δx, which is independent of δk_{rel}, dispersing more k-space per pixel comes at the expense of acquiring fewer k-space samples. As shown in Eq. (2), $S\left(x\frac{1}{\delta k_{rel}}\right)_{int}$ experiences a relatively sparse discrete sampling rate when $\frac{1}{\delta k_{rel}} < \frac{1}{\delta k_{lin}}$. In this way, we show that the k-space sampling rate is proportional to $\frac{1}{\delta k_{rel}}$ (and

Biomedical Optics EXPRESS

estimated by $\frac{1}{\Delta k_{rel}}$). Figure 1(e) shows $S\left(x\frac{1}{\delta k_{rel}}\right)_{int}$ for a segment where $\frac{1}{\delta k_{rel}} > \frac{1}{\delta k_{lin}}$ (highlighted by the orange dot in Fig. 1(a)), where expanded k-space results in a relatively dense k-space sampling rate when $\frac{1}{\delta k_{rel}} > \frac{1}{\delta k_{lin}}$. Other than the spectral distortions described above, uniform sampling by the pixel array itself does not introduce any new distortions (not considering aliasing and roll-off).

2.2. Linear-k interpolation and resampling

A linear-in-k version of $S[j]_{int}$ can be estimated by digitally redistributing the locations of k-space samples. Specifically, $S[j]_{int}$ is interpolated to linear-in-k by calculating unknown values of $S[j]_{int}$ from an estimated continuous version of itself. Due to its simplicity and computational efficiency, a popular SD-OCT fringe interpolation is a linear interpolation (LI) [19], which is the focus of our analysis. However, the mathematical principles and fundamental conclusions derived here remain valid for other interpolations, such as cubic spline. A discrete LI consists of three steps: up-sampling, low-pass filtering, and down-sampling [20].

As shown above, $S[j]_{int}$ is initially down-sampled at shorter wavelengths and up-sampled at longer wavelengths according to $\frac{1}{\delta k_{rel}}$. Phase distortion of $S[j]_{int}$ can be removed by an inverse operation. Therefore, $S[j]_{int}$ is resampled at a rate inverse to $\frac{1}{\delta k_{rel}}$, which is in the up-sampling and down-sampling steps in LI. As illustrated in Fig. 1, LI results in an expansion of shorter wavelengths and compression of longer wavelengths exactly inverse to their original distortions. This can be described mathematically as

$$S[j]_{int\_lin} = \sum_{j=1}^{N} S\left(x\frac{\delta k_{rel}}{\delta k_{rel}}\right)_{int} \theta(x - j\Delta x) = \sum_{j=1}^{N} S(x)_{int}\ \theta(x - j\Delta x). \tag{4}$$

From Eq. (5), the noise-free interference fringe is resampled linearly in k and x, canceling sampling-based distortions. Finally, the low-pass filtering step in LI uses a triangle function

$$t[j] = \begin{cases} 1 - \frac{|j|}{\xi}, & |j| \le \xi \\ 0, & elsewhere \end{cases}, \tag{5}$$

where ξ is the order of interpolation [21]. We show the influence of Eq. (5) in Section 3.3.

2.3. Noise in SD-OCT

In SD-OCT, the additive noise consists of shot noise, dark noise, readout noise, and relative intensity noise (RIN) and is assumed to be Gaussian distributed at each pixel [22]. Unlike sampled fringe $S[j]_{int}$, the additive noise is not correlated with k. Therefore, we modify representation of the signal detected by the spectrometer to

$$S[j]_{total} = S[j]_{int} + e[j]_{noise}, \tag{6}$$

where $e[j]_{noise}$ is the additive noise in SD-OCT.

We confirmed the Gaussian noise distribution by acquiring images using our vis-OCT system (40 μs exposure time, 5000 A-lines, 0.15 μW laser power from reference arm) without any sample in the sample arm. After normalizing the detected noise by the spectral shape of the light source (NKT Photonics, SuperK 150 MHz), we found that our measured noise followed the Gaussian distribution with a mean near 0 and a standard deviation (σ) of 0.79 [arb. Units]. Additionally, it has been shown in SD-OCT that a supercontinuum laser source contributes to pink RIN noise [22]. In our experimental measurements in Section 3, we demonstrate that although pink noises exist, SDBG bias and the general spectral profile of the background is dominated by the white noise component.

Biomedical Optics EXPRESS

2.4. Interpolation of noise in SD-OCT

To understand how interpolation leads to SDBG, we must consider a complete representation of the SD-OCT signal

$$S[j]_{total\_lin} = S[j]_{int\_lin} + e[j]_{noise\_lin} = LI\{S[j]_{int}\} + LI\{e[j]_{noise}\}, \tag{7}$$

where $S[j]_{total\_lin}$ is the linearly interpolated signal detected by the spectrometer; $S[j]_{int\_lin}$ is the linearly interpolated interference fringe; $e[j]_{noise\_lin}$ is the linearly interpolated noise; and LI is the linear interpolation operator. $S[j]_{int}$ and $e[j]_{noise}$ are interpolated independently.

A useful property of white noise is that its autocorrelation is proportional to the Dirac delta function. First, we denote the autocorrelation of $e[j]_{noise}$ as $\phi[j]_{noise_{ee}}$. To investigate $\phi[j]_{noise_{ee}}$ in the same way as the sampled interference fringe, we write $\phi[j]_{noise_{ee}}$ as

$$\phi[j]_{noise_{ee}} = \sum_{j=1}^{N} [e(x) * e(x)]\ \theta(x - j\Delta x) = \sum_{j=1}^{N} \sigma^2 \delta(x)\theta(x - j\Delta x) = \ \sigma^2 \delta[j], \tag{8}$$

where $e(x)_{noise}$ is the SD-OCT noise as a function of continuous space x; $*$ is the continuous convolution operator; σ^2 is the variance of the noise; and $\delta(x)$ and $\delta[j]$ are the continuous and discrete Dirac delta functions, respectively. Equation (8) is valid because $e[j]_{noise}$ is a wide-sense stationary signal [20]. Unlike the interference fringe, neither $e[j]_{noise}$ nor $e(x)$ are correlated with k. As such, from the perspective of the spectrometer array, $e(x)$, $e[j]_{noise}$, and $\phi[j]_{noise_{ee}}$ are all assumed linear with the pixel index. However, interpolating $S[j]_{int}$ still necessitates linear-in-k interpolation of $e[j]_{noise}$. Similar to Eq. (4), we can write the interpolated noise as

$$e[j]_{noise\_lin} = \sum_{j=1}^{N} e(x\delta k_{rel})_{noise}\ \theta(x - j\Delta x). \tag{9}$$

Now, we can write the autocorrelation of the interpolated noise, as

$$\phi[j]_{noise\_lin_{ee}} = \sum_{j=1}^{N} [e(x\delta k_{rel}) * e(x\delta k_{rel})]\ \theta(x - j\Delta x) = \sum_{j=1}^{N} \sigma^2 \delta(x\delta k_{rel})\theta(x - j\Delta x) = \frac{\sigma^2}{\Delta k_{rel}}\delta[j]. \tag{10}$$

Indeed, expansion or compression by δk_{lin} does not linearize k domain sampling for $e[j]_{noise}$ like it does for $S[j]_{int}$. Equation (11) shows that the amplitude of $\phi[j]_{noise\_lin_{ee}}$ is determined by δk_{rel} and scaled by $\frac{1}{\Delta k_{rel}}$.

2.5. SDBG in the reconstructed depth spectrum

Since we are interested in the depth-resolved spectral signatures of vis-OCT signals, we need to investigate the STFT of $S[j]_{total\_lin}$ as

$$STFT\{S[j]_{total\_lin}\} = \sum_{r=1}^{R_{total}} (DFT\{S[\Delta j_r]_{int\_lin}\} + DFT\{e[\Delta j_r]_{noise\_lin}\}), \tag{11}$$

where r is the STFT sub-band spectral window and Δj_r are the sample indexes under the full-width-half-maximum (FWHM) bandwidth of spectral sub-band window r. $S[\Delta j_r]_{int\_lin}$ and $e[\Delta j_r]_{noise\_lin}$ are the windowed versions of $S[j]_{int\_lin}$ and $e[j]_{noise\_lin}$, respectively. We can compute STFT of $\phi[j]_{noise\_lin_{ee}}$ as

$$STFT\{\phi[j]_{noise\_lin_{ee}}\} = \sum_{r=1}^{R_{total}} \frac{1}{j_{end} - j_{start}} \sum_{j=j_{start}}^{j_{end}-1} \frac{\sigma^2 \delta[j]}{\Delta k_{rel_r}} e^{\frac{-i2\pi jz}{j_{end} - j_{start}}} \sim \frac{\sigma^2}{\Delta k_{rel_r}}, \tag{12}$$

where z is the transformed index of j representing the depth; i is the complex number; j_{start} and j_{end} are the first and last indexes of Δj_r, respectively; and Δk_{rel_r} is the windowed version of Δk_{rel}. Applying the Wiener-Khinchen theorem, the DFT of $\phi[j]_{noise\_lin_{ee}}$ for each sub-band is the power

Biomedical Optics EXPRESS

spectral density (PSD) of $e[j]_{noise\_lin}$ under each sub-band, referred to as $\Phi[j]_{noise\_lin_{ee}}$ [20]. Since the result of Eq. (12) is a positive constant for each r, we can relate the PSD to its amplitude spectrum (spectrally dependent A-line or SDA-line: $A[z, \Delta j_r]_{noise\_lin}$) using

$$A[z, \Delta j_r]_{noise\_lin} = \sqrt{\Phi[j]_{noise\_lin_{ee}}} \sim \frac{\sigma}{\sqrt{\Delta k_{rel_r}}}. \tag{13}$$

Then Eq. (11) can be rewritten as

$$STFT\{S[j]_{total}\} = A[z, \Delta j_r]_{int\_lin} + A[z, \Delta j_r]_{noise\_lin}, \tag{14}$$

where $A[z, \Delta j_r]_{int\_lin}$ is an SDA-line reconstructed from the fringe. SDBG is, therefore, a bias of the noise floor proportional to $\frac{1}{\sqrt{\Delta k_{rel_r}}}$.

3. Results

3.1. Simulated SDBG

We simulated SDBG for the Blizzard SR spectrometer by generating a Gaussian white noise ($e[j]_{noise}$) and processing it following an STFT spectroscopic vis-OCT reconstruction procedure [3]. Briefly, we generated $e[j]_{noise}$ with $N = 2048$ pixels and an SD of 0.79 (arb. units, same as measured in Section 2.3). Then, we up-sampled $e[j]_{noise}$ six times using FT zero-padding [19] and linearly resampled to obtain $e[j]_{noise\_lin}$. Finally, we applied STFTs using $R_{total} = 24$ Gaussian windows spaced equidistantly in the k space from 523 nm to 591 nm. Each sub-band had the same FWHM bandwidth, corresponding to a 13-nm FWHM bandwidth for a sub-band centered at 556 nm. We repeated this processing 5000 times with and without the LI step and averaged all the respective $A[z, \Delta j_r]_{noise\_lin}$.

Figure 2(a) shows the simulated $A[z, \Delta j_r]_{noise\_lin}$ with LI after normalizing by its average spectral amplitude $\left(\frac{\sum_{r=1}^{R} A[z,\Delta j_r]_{noise\_lin}}{r}\right)$ and average depth amplitude between z = 500 μm and z = 800 μm $\left(\frac{\sum_{z=500\ \mu m}^{800\ \mu m} A[z,\Delta j_r]_{noise\_lin}}{300\ \mu m}\right)$. From here on, all $A[z, \Delta j_r]_{noise\_lin}$ are plotted after this normalization. The simulated $A[z, \Delta j_r]_{noise\_lin}$ has 24 background values, each representing the r^{th} STFT sub-band. We color-code the central wavelength of each sub-band, as shown by the color bar. Although all $A[z, \Delta j_r]_{noise\_lin}$ are approximately constant with z, the mean amplitude from shorter (green) wavelengths are higher than those from longer (orange) wavelengths. We visualize the simulated SDBG bias in Fig. 2(b) (red dashed line), which we approximate as the depth-averaged $A[z, \Delta j_r]_{noise\_lin}$ between 500 μm and 800 μm:

$$\text{SDBG} \approx A[\Delta j_r]_{noise\_lin} = \frac{\sum_{z=500\ \mu m}^{800\ \mu m} A[z, \Delta j_r]_{int\_lin}}{300\ \mu m} \tag{15}$$

The blue line in Fig. 2(b) shows the SDBG bias predicted by the spectrometer's $\frac{1}{\sqrt{\Delta k_{rel_r}}}$, which agrees well with the simulated $A[\Delta j_r]_{noise\_lin}$. Figure 2(b) and all plotted $A[\Delta j_r]_{noise\_lin}$ are normalized by their average spectral amplitude, as done in Fig. 2(a). We noted that there is a small difference between the SDBG biases at the shortest wavelengths, although this difference is $< 1\%$ of the predicted value. This difference may be caused by σ not being perfectly constant with sub-band center wavelength or a minute depth-dependence of $A[z, \Delta j_r]_{noise\_lin}$, which is discussed in Section 3.3. Figure 2(c) illustrates the simulated $A[z, \Delta j_r]_{noise\_lin}$ after the same respective processing and analysis as Figs. 2(a), without the LI of $e[j]_{noise}$. Figure 2(d) illustrates the simulated $A[\Delta j_r]_{noise\_lin}$ calculated from Fig. 2(c) and the predicted SDBG bias. It is clear that all the noises have the same amplitude, regardless of their center wavelengths. This matches the predicted SDBG bias since $e[j]_{noise}$ is not correlated with k and no k distortion is present.

Biomedical Optics EXPRESS

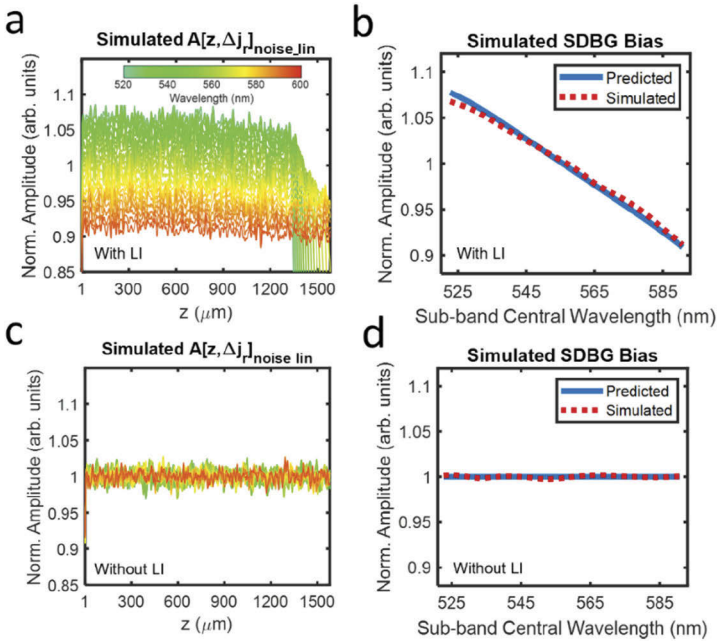

Fig. 2. Simulated SDBGs in vis-OCT. (a) Simulated background SDA-lines with LI; (b) predicted SDBG bias (blue line) and simulated SDBG bias (red dashed line) with LI from z = 500 µm to 800 µm; (c) simulated background SDA-lines without LI; (d) predicted SDBG bias (blue line) and simulated SDBG bias (red dashed line) without LI from z = 500 µm to 800 µm.

3.2. *Experimentally measured SDBG*

We applied the same analysis from Section 3.1 to experimentally acquired $e[j]_{noise}$ using our vis-OCT system. Figure 3(a) shows the $A[z, \Delta j_r]_{noise\_lin}$ from the measured $e[j]_{noise}$, plotted using the same colorbar in Fig. 2(a). The experimental $A[z, \Delta j_r]_{noise\_lin}$ in Fig. 3(a) has a similar, monotonic spectral bias to that of the simulated version (Fig. 2(a)). We confirmed this trend by measuring $A[\Delta j_r]_{noise\_lin}$ (Fig. 3(b), red dashed line). Similar to the simulated $A[\Delta j_r]_{noise\_lin}$, the experimental $A[\Delta j_r]_{noise\_lin}$ (also for depths 500 μm – 800 μm) decreases approximately linearly with increasing central wavelength. Unlike the simulated $A[z, \Delta j_r]_{noise\_lin}$, the experimental $A[z, \Delta j_r]_{noise\_lin}$ (Fig. 3(a)) is not approximately constant with depth. Instead, its amplitudes are higher at shorter depths and decay exponentially with depth, which may be caused by two experimental conditions. First, the noise distribution from a supercontinuum laser is pink [22], which contains a higher proportion of low-frequency noises. Second, imperfect normalization of the light source spectral shape can propagate a low-frequency component into interference fringe. As shown in Eq. (10), the SDBG bias is contingent on the spectroscopic processing of white noise. To this end, it was important to directly measure $A[z, \Delta j_r]_{noise\_lin}$ to monitor any inconsistencies with the model. Since the measured SDBG bias was in strong agreement with our mathematical model and simulation, we concluded, to a reasonable approximation, that background noise in our vis-OCT system was dominated by a white noise process and interpolation. We did note small differences (~ 2% error) between the measured $A[\Delta j_r]_{noise\_lin}$ and predicted SDBG bias, which was likely explained by the lower noise frequencies, normalization of the light source shape, or σ not being perfectly constant across spectral locations, which may be caused by different excess noises or efficiencies of the spectrometer elements [23]. Since supercontinuum laser sources may vary in power, spectral shape, repetition rate, and RIN noise, it is important that researchers

Biomedical Optics EXPRESS

directly measure the SDBG. They may also directly investigate light-dependent influences by comparing the SDBG with the light source on and off.

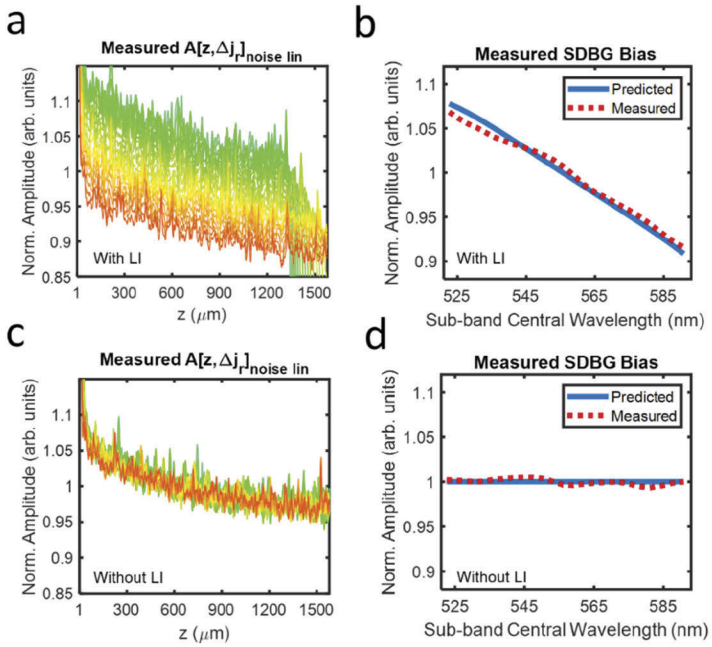

Fig. 3. Measured SDBGs in vis-OCT. (a) Measured background SDA-lines with LI; (b) predicted SDBG bias (blue line) and measured SDBG bias (red dashed line) with LI from z = 500 μm to 800 μm; (c) measured background SDA-lines without LI; (d) predicted SDBG bias (blue line) and measured SDBG bias (red dashed line) without LI from z = 500 μm to 800 μm

Finally, Figs. 3(c) and 3(d) illustrate the measured $A[z, \Delta j_r]_{noise\_lin}$ and $A[\Delta j_r]_{noise\_lin}$, respectively, without LI. As predicted, the spectral dependence of the background noise floor is not present. Furthermore, depth decay of the background still existed since the frequency distribution of the background noise is not influenced by interpolation.

3.3. *Influence of interference fringe up-sampling*

To this point, to simplify the calculation of SDBG, we did not extend the analysis to the filter in Eq. (5). Indeed, the convolution of $t[j]$ with $e[j]_{noise}$ adds additional depth-dependence and spectral dependence to the SDBG. The STFT of $t[j]$ for LI is

$$T[z, \Delta j_r] = sinc^2\left[\frac{z\Delta k_{relr}}{\pi}\right], \tag{16}$$

where ξ from Eq. (5) is set to 1 since the total number of samples in each sub-band does not change. The multiplication of Δk_{rel} with z signifies the scaling of the k domain after resampling. Therefore, true SDA-line can be written as

$$STFT\{S[j]_{total}\} = A[z, \Delta j_r]_{int\_lin} T[z, \Delta j_r] + A[z, \Delta j_r]_{noise\_lin} T[z, \Delta j_r] \tag{17}$$

which adds the spectrally-dependent roll-off (SDR) [17] component to the signal and noise, according to Eq. (16). It has been shown that uniformly up-sampling $S[j]_{total}$ before the interpolation step reduces A-line amplitude decay with depth [19]. This is because up-sampling

Biomedical Optics EXPRESS

compresses SDA-lines, but not the depth-resolved interpolation filter. Compression of imaging depths relative to the interpolation filter exposes them to less decay by the $sinc^2$ function than without compression (no up-sampling).

If $S[j]_{total}$ is up-sampled at a high enough rate, the SDR induced by the interpolation filter becomes small enough to be negligible for most applications. This is also why there is no visually noticeable decay by the $sinc^2$ function in Fig. 3. However, to our knowledge, an optimal up-sampling rate for spectroscopic vis-OCT has not been determined. An optimal up-sampling rate should be established since researchers may apply low upsampling rates to increase processing speeds without considering the spectroscopic consequences.

We investigate a minimum upsampling rate for spectroscopic vis-OCT in Fig. 4, which uses the simulation from Fig. 2(a), except that we varied the up-sampling rates before interpolation. We compared $A[z, \Delta j_r]_{noise\_lin}T[z, \Delta j_r]$ corresponding to upsampling rates of 1, 2, 4, and 6. In Fig. 4(a), $A[z, \Delta j_r]_{noise\_lin}T[z, \Delta j_r]$ is influenced by the depth-independent amplitude scaling in Eq. (13) and the depth-dependent interpolation filter in Eq. (16). Each noise component decays with depth, where shorter wavelengths decay more rapidly than longer ones. Such decay adds two additional influences to the noise floor: decay with depth and different depth decay rates with different wavelengths. These influences further complicate the alterations of spectroscopic vis-OCT measurements since the assumption of a constant SDBG bias shown in Eq. (13) is no longer satisfied. This also complicates the SDBG correction, which is described in Section 3.4. As shown in Figs. 4(b) and 4(c), the influence of the interpolation filter is reduced with increased upsampling but cannot be completely removed. Under six-fold up-sampling (Fig. 4(d)), $A[z, \Delta j_r]_{noise\_lin}T[z, \Delta j_r]$ only shows minute decay with depth, which suggests that $S[j]_{total}$ should be up-sampled at least six times. At this point, Eq. (17) can be simplified back to Eq. (14). Finally, we note that $T[z, \Delta j_r]$ is also multiplicative with the signal-carrying SDA-lines in Eq. (17). Up-sampling $S[j]_{total}$ by six-fold will reduce SDR of the signal-carrying SDA-lines in the same way as the background shown in Fig. 4.

3.4. Correcting SDBG in vis-OCT oximetry in humans

Influence of SDBG on spectroscopic analysis can be corrected experimentally by subtracting $A[z, \Delta j_r]_{int\_lin}$ from Eq. (14) as

$$A[z, \Delta j_r]_{int\_lin} = STFT\{S[j]_{total}\} - A[z_0, \Delta j_r]_{noise\_lin} \tag{18}$$

where z_0 is the depth of the spectroscopic calculation. Practically, this can be accomplished by selecting a depth region where the spectroscopic image is completely attenuated. Since the experimental SDBG was shown to decay with depth, we fit an exponential curve to each $A[z, \Delta j_r]_{noise\_lin}$ in the selected depth region. We then used the fitted values at z_0 to estimate $A[z_0, \Delta j_r]_{noise\_lin}$. We note that zero-padding the fringe at least 6-fold greatly simplifies this correction since the depth decays of the SDBG are minimized and nearly uniform across all spectral sub-bands. Insufficient zero-padding, as exemplified in Fig. 4(a), introduces additional complications: (1) The assumption of simple exponential decay is lost according to Eq. (16); and (2) Each sub-band experiences a unique, spectrally-dependent decay, leaving them more susceptible to errors from direct measurement or depth-fitting of the SDBG. If the spectroscopic image is not completely attenuated, it is an acceptable alternative to acquiring only the background signal, as shown in Fig. 3(a), and directly calculate $A[z_0, \Delta j_r]_{noise\_lin}$. However, this will also require the researcher to account for any other modifications made in the spectroscopic image processing, which is discussed in Section 4.

To demonstrate the importance of SDBG correction, we measured the vis-OCT spectrum of blood in human retinal vessels. Briefly, we imaged the retina of a healthy 23-year-old volunteer with a vis-OCT system described in [24]. Human imaging was approved by the Northwestern University Institutional Review Board and adhered to the Declaration of Helsinki. The optical

Biomedical Optics EXPRESS

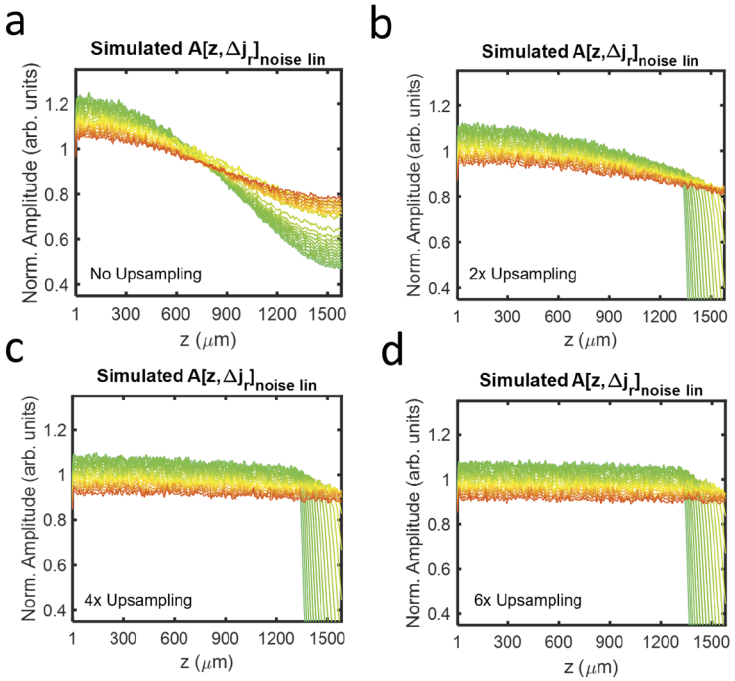

Fig. 4. Simulated background SDA-lines with LI after (a) no, (b) two-fold, (c) four-fold, and (d) six-fold up-sampling.

power incident on the cornea was 250 μW. We measured the spectrum inside the retinal blood vessels using STFT sub-bands $r = 3$ to $r = 23$ (528 nm to 588 nm). We applied standard OCT processing, including removal of the spectrum DC component, 6-fold zero-padding, compensation for dispersion mismatch, and correction for the system roll-off. We averaged ~ 500 pixels in each vessel from 16 B-scans (8192 A-lines per B-scan) to reduce the background and speckle noise fluctuations.

We calculated the influence of SDBG in an artery (red box) and vein (blue box), as highlighted in Fig. 5(a), near the optic disk. The spectrum was detected at an average distance of ~40 μm below the anterior vessel wall and is plotted in blue in Fig. 5(b). All spectra are plotted after normalizing by their respective mean amplitudes. The red dashed-line in Fig. 5(b) is the predicted spectrum from the literature [25] for oxygen concentration (sO_2) = 100%. Note how the blue spectrum is tilted downwards with increasing wavelength and does not well match the literature spectrum. Figure 5(c) shows the measured $A[z_0, \Delta j_r]_{noise\_lin}$. It matches well with those simulated and experimental SDBGs shown in Figs. 2(b) and 3(b). The downwards tilt in the measured spectrum in Fig. 5(b) follows the trend of $A[z_0, \Delta j_r]_{noise\_lin}$ in Fig. 5(c).

Figure 5(d) shows the same spectral calculation in Fig. 5(b) after SDBG correction. We corrected the spectrum using $A[z_0, \Delta j_r]_{noise\_lin}$ from Fig. 5(c). After correction, the spectrum matches well ($R^2 = 0.98$) with the literature spectrum ($sO_2 = 100\%$). Figure 5(e) shows the measured spectrum (blue line) without SDBG correction in the vein and literature spectrum (red dashed-line) for $sO_2 = 60\%$. Again, the measured spectrum differs from the literature spectrum with a tilt downwards at longer wavelengths. Figure 5(f) shows the measured $A[z_0, \Delta j_r]_{noise\_lin}$. Figure 5 g shows the SDBG corrected spectrum, which well agrees with the literature spectrum ($R^2 = 0.98$).

Biomedical Optics EXPRESS

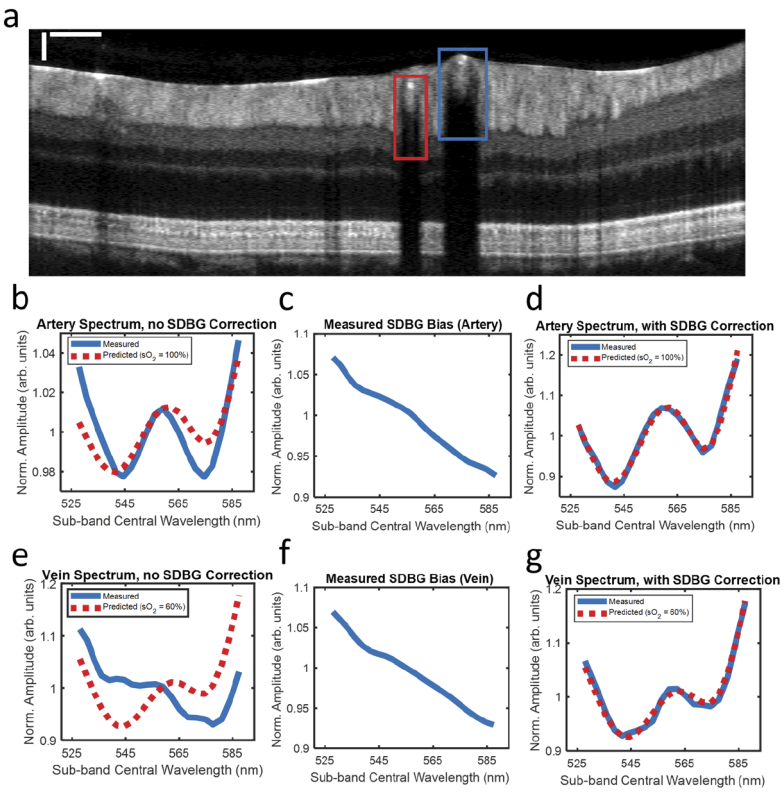

Fig. 5. SDBG correction in the human retina. (a) B-scan image with one artery (red box) and one vein (blue box); scale bars are 250 μm (lateral) and 50 μm (axial); (b) measured blood spectrum in the artery before SDBG correction; (c) measured SDBG bias in the artery; (d) measured blood spectrum in the artery after SDBG correction; (e) measured blood spectrum in the vein before SDBG correction; (f) measured SDBG bias in the vein; (g) measured blood spectrum in the vein after SDBG correction.

3.5. Metric to evaluate the influence of SDBG on spectroscopic OCT measurements

We recognized that the influence of SDBG also depends on the amplitude of the spectroscopic signal relative to the noise floor. To quantify SDBG's influence on retinal oximetry in vessels similar to the ones in Fig. 5, we simulated oxygen-dependent spectra for $sO_2 = 0$ to 100% and SDBGs for different signal-to-noise-floor-ratios (SNFRs). We define SNFR as

$$SNFR = \frac{\sum_{r=1}^{R} A[z_0, \Delta j_r]_{int\_lin}/r}{\sum_{r=1}^{R} A[z_0, \Delta j_r]_{noise\_lin}/r}, \tag{19}$$

which is the ratio between the mean spectral amplitudes from the structure of interest and the noise floor. We calculated sO_2 from the simulated spectra and calculated the root-mean-squared-error (RMSE) between the calculated sO_2 and the ground truth. Figure 6 illustrates RMSE from the computer-generated ground truth when SNFR varies from 3 to 100 (sO_2 values for SNFRs below 3 could not be quantified). Indeed, the error of sO_2 is severely compromised by SDBG until SNFR > 55 (RMSE < 2%). For our vis-OCT setup, we found that typical SNFR in locations used for sO_2 were no higher than 5, which was limited by the rapid attenuation of blood. The SNFRs in Fig. 5(a) were 2.05 and 1.77 for the artery and vein, respectively. The sO_2 could not be calculated in these vessels until the SDBG was corrected. Therefore, we conclude that

Biomedical Optics EXPRESS

SDBG correction is critical for human retinal oximetry. The influence of SDBG correction will be different depending on specific applications. We recommend readers to simulate an accuracy metric similar to that shown in Fig. 6 to quantify the influence of the SDBG in a specific application.

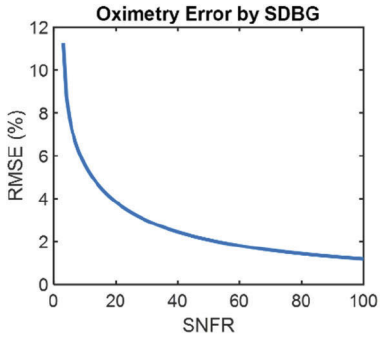

Fig. 6. RMSE of simulated sO_2 measurements with respect to the ground truth as a function of SNFR.

4. Discussion

We thoroughly investigated a systemic SDBG in spectroscopic SD-OCT. We developed a mathematical model to show that SDBG is caused by linear-in-k interpolation of the white noise. We validated the model using simulated and experimental SDBGs in vis-OCT. We demonstrated the importance of up-sampling the fringe before LI. We corrected SDBG in human spectroscopic vis-OCT and found that correcting SDBG was critical for measuring an accurate blood spectrum in humans. Finally, we showed the influence of SDBG in spectroscopic SD-OCT under different SNFR levels.

Potentially most insidious are cases where measured spectra agree with their literature models but are still subject to SDBG bias. Indeed, the SDBG amplitude derived here monotonically decreases with wavelength. Such shape is inconveniently correlated with the reported $\lambda^{-\alpha}$ scattering and backscattering spectra of many biological tissues, where α is a constant [4,26]. As such, perceived scattering properties of tissue may be altered by the SDBG. This is relevant in a model of light-tissue interaction where the scattering coefficient or elements of the scattering coefficient a fitted parameter [13].

We note that δk_{rel} varies more in visible-light spectral range than in NIR spectral range. To this end, the SDBG is likely to influence spectroscopic vis-OCT applications the most. Using a linear-in-k spectrometer [27] or swept-source [16] (not currently available in visible light), rather than a grating-based spectrometer, will greatly reduce the influence of SDBG since δk_{rel} becomes nearly constant. In this work, we performed all STFT analysis using sub-bands with uniform bandwidths in k space. Varying sub-bands' bandwidths in the STFT to compensate for SDBG remains an open question. However, doing so will alter the amplitudes and resolutions of $A[z, \Delta j_r]_{int\_lin}$. Finally, we recognize that in spectroscopic OCT, the interference fringe is often divided by the source spectrum, $\sqrt{S_{samp}(k,z)S_{ref}(k)}$ from Eq. (1), for normalization purposes. As such, the measured SDBG may be altered by $\sqrt{S_{samp}(k,z)S_{ref}(k)}$, depending on normalization method and SDBG amplitude. However, such normalization does not alter the analysis concluded in this work, nor does it alter the proposed SDBG correction.

Finally, while this work focused on LI, more sophisticated interpolations, such as spline, which trade speed and simplicity for better roll-offs, are of interest to researchers based on application. We confirmed that our SDBG analysis is consistent with other interpolations. In

Biomedical Optics EXPRESS

the Appendix, Fig. 7(a) illustrates the SDBG for simulated noise using spline interpolation, and Fig. 7(b) illustrates the SDBG for measured noise using spline interpolation. The plots were generated using the same methods that generated Figs. 2(a) & 3a, respectively. Indeed, the SDBGs generated using spline interpolation are nearly identical to those generated using LI. This is because the SDBG bias is principally dependent on the resampling of white noise shown in Eq. (13). Since spline interpolation has less roll-off than LI [20], it required only 2-fold upsampling to reach the constant bias derived in Eq. (13) and seen in Fig. 7(a), as opposed to 6-fold for LI, as shown in Fig. 4. Researchers can use the tools provided in this work to assess which interpolation technique best fits their application of spectroscopic OCT.

5. Conclusion

In conclusion, we demonstrated that spectroscopic SD-OCT signals are intrinsically biased by the spectrometer's k spacing after linear-in-k interpolation. We investigated this phenomenon in vis-OCT and found strong agreements between mathematical modeling, simulation, and experiment. We found that correction of the SDBG is important for retinal oximetry, a primary application for vis-OCT. By establishing and verifying the principles of the SDBG, this work informs researchers towards making accurate spectroscopic OCT measurements.

Appendix

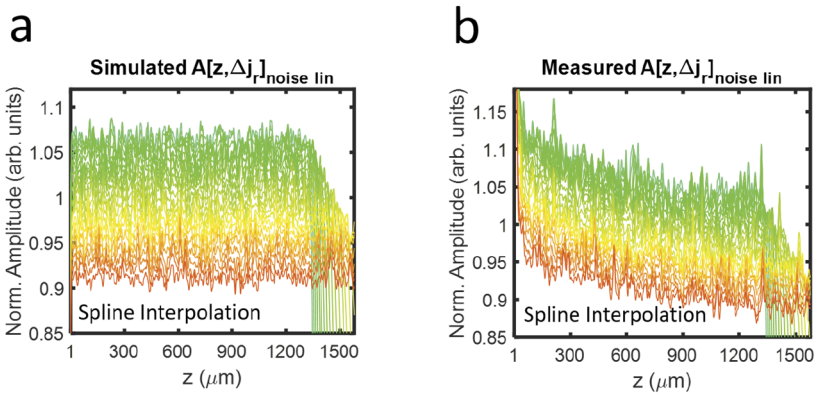

Fig. 7. SDBGs in vis-OCT using spline interpolation. (a) Simulated background SDA-lines with spline interpolation; (b) Measured background SDA-lines with spline interpolation.

Funding

National Institutes of Health (R01EY019949, R01EY026078, R01EY028304, R01EY029121, R44EY026466, T32EY25202).

Acknowledgments

The authors thank David A. Miller and Lisa Beckmann for helpful discussions.

Disclosures

RVK and HFZ have financial interests in Opticent Health.

Biomedical Optics EXPRESS

References

1. D. Huang, E. A. Swanson, C. P. Lin, J. S. Schuman, W. G. Stinson, W. Chang, M. R. Hee, T. Flotte, K. Gregory, C. A. Puliafito, and J. G. Fujimoto, "Optical Coherence Tomography," Science **254**(5035), 1178–1181 (1991).
2. J. A. Izatt and M. A. Choma, "Theory of Optical Coherence Tomography," *Optical Coherence Tomography: Technology and Applications*, 47–72 (2008).
3. X. Shu, L. Beckmann, and H. F. Zhang, "Visible-light optical coherence tomography: a review," J Biomed Opt **22**(12), 121707 (2017).
4. J. Yi, Q. Wei, W. Z. Liu, V. Backman, and H. F. Zhang, "Visible-light optical coherence tomography for retinal oximetry," Opt. Lett. **38**(11), 1796–1798 (2013).
5. F. E. Robles, C. Wilson, G. Grant, and A. Wax, "Molecular imaging true-colour spectroscopic optical coherence tomography," Nat. Photonics **5**(12), 744–747 (2011).
6. R. R. Liu, J. A. Winkelmann, G. Spicer, Y. X. Zhu, A. Eid, G. A. Ameer, V. Backman, and J. Yi, "Single capillary oximetry and tissue ultrastructural sensing by dual-band dual-scan inverse spectroscopic optical coherence tomography," Light: Sci. Appl. **7**(1), 57 (2018).
7. L. Beckmann, X. Zhang, N. A. Nadkarni, Z. Cai, A. Batra, D. P. Sullivan, W. A. Muller, C. Sun, R. Kuranov, and H. F. Zhang, "Longitudinal deep-brain imaging in mouse using visible-light optical coherence tomography through chronic microprism cranial window," Biomed. Opt. Express **10**(10), 5235–5250 (2019).
8. A. Lichtenegger, D. J. Harper, M. Augustin, P. Eugui, M. Muck, J. Gesperger, C. K. Hitzenberger, A. Woehrer, and B. Baumann, "Spectroscopic imaging with spectral domain visible light optical coherence microscopy in Alzheimer's disease brain samples," Biomed. Opt. Express **8**(9), 4007–4025 (2017).
9. Z. L. Hu, Y. S. Pan, and A. M. Rollins, "Analytical model of spectrometer-based two-beam spectral interferometry," Appl. Opt. **46**(35), 8499–8505 (2007).
10. C. Dorrer, N. Belabas, J. P. Likforman, and M. Joffre, "Spectral resolution and sampling issues in Fourier-transform spectral interferometry," J. Opt. Soc. Am. B **17**(10), 1795–1802 (2000).
11. B. Baumann, C. W. Merkle, R. A. Leitgeb, M. Augustin, A. Wartak, M. Pircher, and C. Hitzenberger, "Signal averaging improves signal-to-noise in OCT images: But which approach works best, and when?" Biomed. Opt. Express **10**(11), 5755–5775 (2019).
12. B. Baumann, M. Augustin, A. Lichtenegger, D. J. Harper, M. Muck, P. Eugui, A. Wartak, M. Pircher, and C. K. Hitzenberger, "Polarization-sensitive optical coherence tomography imaging of the anterior mouse eye," J. Biomed. Opt. **23**(08), 1 (2018).
13. C. Veenstra, S. Kruitwagen, D. Groener, W. Petersen, W. Steenbergen, and N. Bosschaart, "Quantification of total haemoglobin concentrations in human whole blood by spectroscopic visible-light optical coherence tomography," Sci. Rep. **9**(1), 15115 (2019).
14. M. Szkulmowski and M. Wojtkowski, "Averaging techniques for OCT imaging," Opt. Express **21**(8), 9757–9773 (2013).
15. S. P. Chong, C. W. Merkle, C. Leahy, H. Radhakrishnan, and V. J. Srinivasan, "Quantitative microvascular hemoglobin mapping using visible light spectroscopic Optical Coherence Tomography," Biomed. Opt. Express **6**(4), 1429–1450 (2015).
16. M. Wojtkowski, "High-speed optical coherence tomography: basics and applications," Appl. Opt. **49**(16), D30–D61 (2010).
17. I. Rubinoff, B. Soetikno, D. A. Miller, I. Rischall, A. Fawzi, R. Kuranov, and H. F. Zhang, "Spectrally dependent roll-off in visible-light optical coherence tomography," Opt. Lett. **45**(9), 2680–2683 (2020).
18. N. Uribe-Patarroyo, S. H. Kassani, M. Villiger, and B. E. Bouma, "Robust wavenumber and dispersion calibration for Fourier-domain optical coherence tomography," Opt. Express **26**(7), 9081–9094 (2018).
19. S. W. Lee, H. W. Jeong, B. M. Kim, Y. C. Ahn, W. Jung, and Z. P. Chen, "Optimization for Axial Resolution, Depth Range, and Sensitivity of Spectral Domain Optical Coherence Tomography at 1.3 mu m," J. Korean Phys. Soc. **55**(6), 2354–2360 (2009).
20. A. V. Oppenheim and R. W. Schafer, *Discrete-time signal processing*, 3rd ed. (Pearson, 2010), pp. xxviii.
21. P. Laguna, G. B. Moody, and R. G. Mark, "Power spectral density of unevenly sampled data by least-square analysis: Performance and application to heart rate signals," IEEE Trans. Biomed. Eng. **45**(6), 698–715 (1998).
22. M. Jensen, I. B. Gonzalo, R. D. Engelsholm, M. Maria, N. M. Israelsen, A. Podoleanu, and O. Bang, "Noise of supercontinuum sources in spectral domain optical coherence tomography," J. Opt. Soc. Am. B **36**(2), A154–A160 (2019).
23. S. P. Chong, M. Bernucci, H. Radhakrishnan, and V. J. Srinivasan, "Structural and functional human retinal imaging with a fiber-based visible light OCT ophthalmoscope," Biomed. Opt. Express **8**(1), 323–337 (2017).
24. I. Rubinoff, L. Beckmann, Y. B. Wang, A. A. Fawzi, X. R. Liu, J. Tauber, K. Jones, H. Ishikawa, J. S. Schuman, R. Kuranov, and H. F. Zhang, "Speckle reduction in visible-light optical coherence tomography using scan modulation," Neurophotonics **6**(04), 1 (2019).
25. D. J. Faber, M. C. G. Aalders, E. G. Mik, B. A. Hooper, M. J. C. van Gemert, and T. G. van Leeuwen, "Oxygen saturation-dependent absorption and scattering of blood," Phys. Rev. Lett. **93**(2), 028102 (2004).

Biomedical Optics EXPRESS

26. J. Yi, A. J. Radosevich, J. D. Rogers, S. C. P. Norris, I. R. Capoglu, A. Taflove, and V. Backman, "Can OCT be sensitive to nanoscale structural alterations in biological tissue?" Opt. Express **21**(7), 9043–9059 (2013).
27. G. P. Lan and G. Q. Li, "Design of a k-space spectrometer for ultra-broad waveband spectral domain optical coherence tomography," Sci Rep-Uk **7**(1), 42353 (2017).